Directed Self-Assembly at the 10-nm Scale by Using Capillary-Force-Induced Nanocohesion

Huigao Duan[1, 2], Karl K. Berggren[1, *]

[1] Department of Electrical Engineering and Computer Science, Massachusetts Institute of Technology, Cambridge, MA 02139, USA

[2] School of Physical Science and Technology, Lanzhou University, Lanzhou, Gansu 730000, P. R. China

[*] To whom correspondence should be addressed, E-mail: berggren@mit.edu

ABSTRACT We demonstrated a new nanoassembly strategy based on capillary-force-induced cohesion of high-aspect-ratio nanostructures made by electron-beam lithography. Using this strategy, ordered complex pattern were fabricated from individual nanostructures at the 10-nm length scale. This method enables the formation of complex designed networks from a sparse array of nanostructures, suggesting a number of potential applications in fabrication of nanodevices, nanopatterning, and fluid-flow investigations.

KEYWORDS Capillary force, self-assembly, nanocohesion, electron-beam lithography, 10-nm-scale.

Capillary force plays a dominant role in a large range of natural phenomena[1-8], and has been widely used as a driving force for the self-assembly of nanoscale to mesoscale objects[9-18]. However, these self-assembly processes based on capillary forces were limited to the microscale and mesoscale and have never been used in patterning sub-100-nm-length-scale structures. Furthermore, local control of self-assembly on this length scale had not been achieved. In this report, we demonstrate a directed-assembly process based on controllable capillary-force-induced nanocohesion that can precisely assemble individual high-aspect-ratio structures at 10-nm-length scales into complex hierarchical structures.

The basic idea of this nanoassembly process is shown in Fig. 1a, where straight high-aspect-ratio nanopillars are first defined as latent features in resist and then developed in a liquid developing agent. In the subsequent drying process, capillary force exists between the nanopillars on the nanopillar-liquid-air interface[2, 19]. When the capillary force is larger than a critical force[19, 20], the nanopillars will collapse, potentially resulting in nanocohesion. If the adhesion force between the cohered pillars is larger than the elastic force of pillars, the cohesion would sustain after drying. By adjusting the spatial distribution of nanopillars, this cohesion can be used to form complex two-dimensional structures at the 10-nm lengthscale.

An example of this process is shown in Figs. 1b and 1c, where we fabricated two arrays of uniformly-distributed high-aspect-ratio negative PMMA nanopillars[21] using the same parameters, but dried one of them by using a supercritical-point carbon dioxide dryer (for Fig. 1b) and the other by using a spin dryer (for Fig. 1c). The diameter of the pillars was ~15 nm, the height was ~80 nm, and the pitch was 50 nm. In Fig. 1b, all of the high-aspect-ratio nanopillars remained standing because the supercritical-point drying process eliminated the surface tension and resultant capillary force; while in Fig. 1c, all of the pillars collapsed and cohered into various assemblies because of the capillary force induced in the liquid-evaporation process.

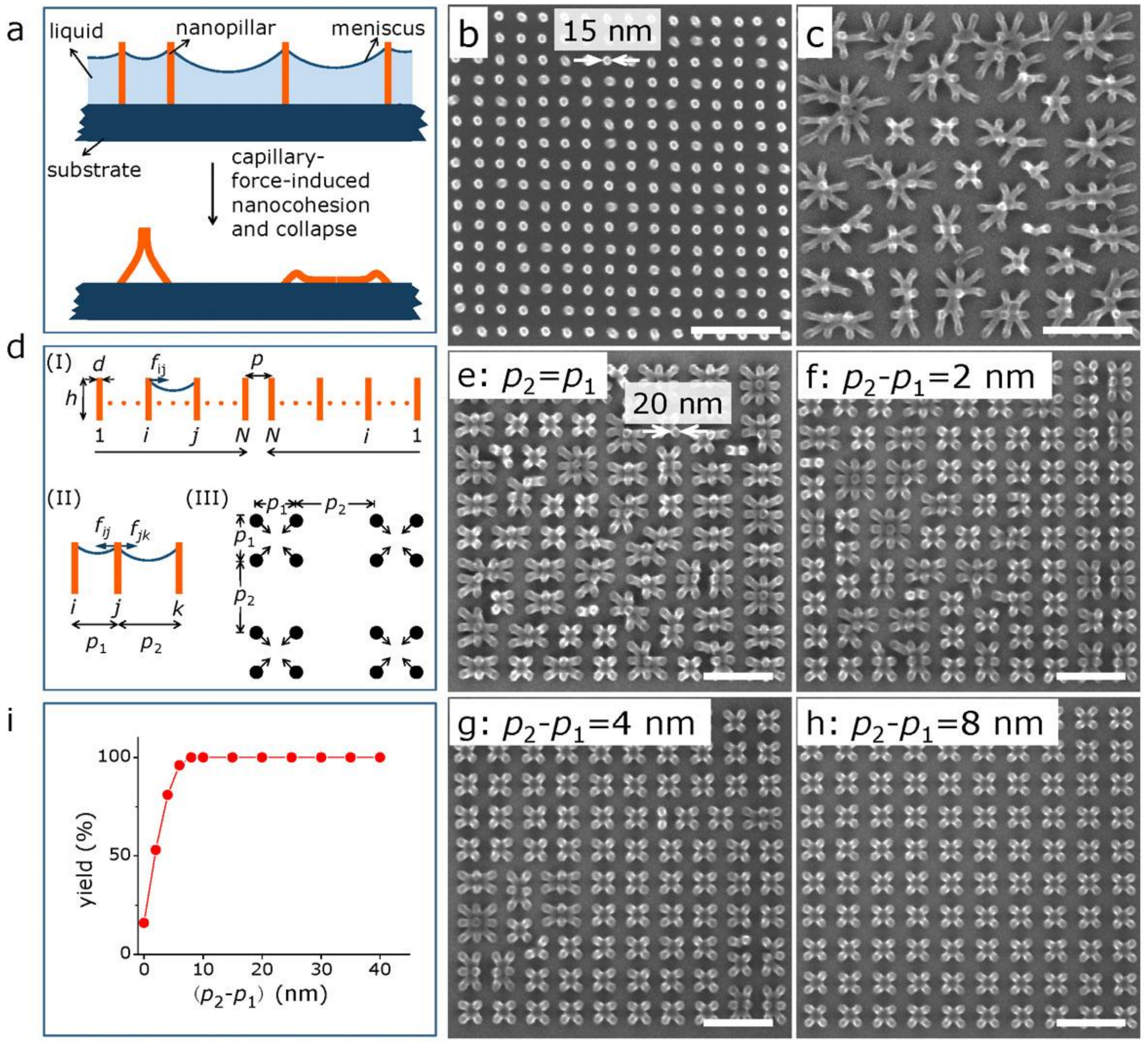

Figure 1. Schematics of controllable capillary-force-induced nanocohesion process. (**a**) Schematic of nanoassembly by capillary-force-induced cohesion of high-aspect-ratio nanostructures in the drying process. (**b**) Scanning-electron microscopy (SEM) image of 50-nm-pitch nanopillars with diameter ~ 15 nm fabricated by electron-beam lithography using poly(methyl methacrylate) (PMMA) as a negative resist. The thickness of PMMA was ~ 90 nm, the lithographic electron dose for each individual pillar was 300 fC, and the resultant height of nanopillars was ~ 80 nm. The sample was developed by 1:2 Methyl isobutyl ketone (MIBK): isopropyl alcohol (IPA) for 1 min at 20 °C, rinsed by pure IPA, and then dried in a supercritical point dryer. (**c**) SEM image of negative PMMA nanopillars

dried in a spin dryer in air at room temperature, in which pattern collapse was induced by capillary forces in the liquid-evaporation process. The nanopillars were fabricated by using the same parameters as those in (b). (**d**) Schematic of (I) a one-dimensional uniform 2N-nanopillar array, (II) 3-pillar array, and (III) a two-dimensional nanopillar array with designed capillary force to direct the pattern collapse. In (III), p_1 is the pitch of nanopillars in the same cell and p_2 is defined as the intercell spacing of two adjacent cells. When $p_2 \neq p_1$, asymmetric capillary forces will be introduced. (**e-h**) SEM images of cohered nanopillars with $p_2 = p_1$ (e), $p_2 - p_1 = 2$ nm (f), $p_2 - p_1 = 4$ nm (g), $p_2 - p_1 = 8$ nm (h), demonstrating that the yield of deterministic cohesion increased when increasing intercell spacing p_2. The diameter of nanopillars was ~ 20 nm, the pitch of pillars in the cell p_1 was 50 nm, and the lithographic electron dose for each individual pillar was 400 fC. (**i**) Quantitative yield as a function of the value of intercell spacing variation ($p_2 - p_1$), which shows high yield of deterministic cohesion when ($p_2 - p_1$) was large enough. All SEM images show the full extent of the patterned region, and their scale bars are 200 nm.

Similar capillary-force-induced collapse effects have been widely reported as unwanted random behaviors in many high-aspect-ratio structures such as carbon nanotubes[22], ZnO nanowires[23], silicon nanorods[24], polymer micropillars[25], and general resist structures[8, 26]. In these cases, the random collapse is thought to result from the combination of many factors[27] such as capillarity, self-weight[28], anisotropic geometry[29], and even a domino effect[18, 30]. To direct the collapse, we must use one of these factors as the main driving force. Recently, domino-effect-based[30], gel-assisted[31], and asymmetric-geometry-based[29] self-organizations of nanopillars or microneedles have been reported. However, these self-organization processes still cannot be well controlled or designed to achieve arbitrary two- or three-dimensional nanostructures.

In this work, we used intentionally-asymmetric capillary forces to reproducibly direct the self-assembly of nanopillars to form ordered, designable nanostructures. Comparing to previous work, our study focused on how to control the capillary-force-induced self-assembly of high-aspect-ratio structures at 10-nm-length scales. By locally varying the initial relative positions and tuning the critical minimum cohesion force of structures, complex hierarchical patterns were fabricated from sparse individual lithographically-defined posts.

The capillary force between two pillars *i* and *j* is given by

$$f_{ij} = 2\pi\, S_{ij}\, \gamma \cos\alpha / p_{ij} \qquad (1)$$

where S_{ij} is the effective surface area contributing to capillary force, γ is the surface tension of liquid, α is the contact angle between liquid and the pillars, and p_{ij} is the distance between pillars *i* and *j* prior to collapse[32]. The net force on an individual pillar *i* in a pillar array is the sum of capillary forces from all other pillars.

To simplify the description, we consider the situation shown in Fig. 1d(I) of a one-dimensional uniform symmetric series of 2N pillars (for odd numbers of pillars, the capillary force for the middle pillar is zero due to symmetry). In this case, the total capillary force for the pillar *i* is given by

$$f_i = 2\pi\gamma\cos\alpha \sum_{j=1,\neq i}^{2\mathrm{N}} S_{ij} \frac{1}{(j-i)p} \quad (1 \le i \le \mathrm{N},\ 1 \le j \le 2\mathrm{N}) \qquad (2)$$

where p is the pitch of this pillar array, S_{ij} can be considered as the effective surface area contributing to capillary force between pillars *i* and *j*, which decreases when increasing the distance between pillars *i* and *j*.

Due to the symmetry of the system, many terms cancel out and we can simplify the equation (2) to get the asymmetric capillary force for each pillar:

$$f_i = 2\pi\gamma\cos\alpha \sum_{j=2i}^{2\mathrm{N}} S_{ij} \frac{1}{(j-i)p} \quad (1 \le i \le \mathrm{N},\ 1 \le j \le 2\mathrm{N}) \qquad (3)$$

From this equation, we know that, for a fixed pillar-number 2N, boundary pillars (i=1) have the largest asymmetric capillary force, and the asymmetric capillary force applied on the pillar i decreases when it is closer to the middle (i.e., increasing i to N), while the central pillars have the smallest asymmetric capillary force (i=N). There exists a critical minimum lateral force f_{min} to collapse a pillar[19, 20]. When $f_{\mathrm{i}} > f_{\mathrm{min}}$, the pillar i will collapse in the direction of the capillary force; when $f_{\mathrm{i}} < f_{\mathrm{min}}$, the pillar i will remain vertical. Thus the pillars closer to the boundary prefer to collapse toward the center, while the pillars closer to the middle prefer to stand. In an ideal infinitely-uniform pillar array, no pillar will collapse because the capillary forces for any pillar equilibrate to zero. In reality, there exist other random facts such as pillar displacement, intrinsic imperfections of pillars, and the dynamics of dewetting, which could introduce random deformation or collapse of some pillars. In particular, these initial random deformations or collapses could break the symmetry of the surroundings and induce dynamic effects.

The scenario shown in Fig. 1c can thus be understood to be determined by the combined effects described above, in which boundary pillars had enough asymmetric capillary force towards the center of the array, so they collapsed to the center, but inner pillars collapsed randomly because the directed capillary forces were insufficient and thus their collapse was determined by random effects.

To direct collapse of all pillars, the asymmetric capillary force f_{i} of all the pillars must be larger than f_{min}. There are two possible ways to achieve this result: (1) by increasing asymmetric capillary force for all pillars; and (2) by decreasing the minimum critical collapse force f_{min}. We will discuss each of these possible approaches.

To demonstrate control and strengthening of the asymmetric capillary force, we introduced asymmetric design in a pillar array to achieve designed force on all pillars. The schematic of our simplest method is shown in Fig. 1d(II), where the capillary force of the center pillar is

$$f_j = f_{ij} - f_{jk} = 2\pi S\gamma \cos\alpha / p_1 - 2\pi S\gamma \cos\alpha / p_2 \sim (1/p_1 - 1/p_2) = (p_2 - p_1)/p_1 p_2 \quad (4)$$

When the pitch difference of $p_2 - p_1$ is much smaller than $p_1 p_2$, $f_j \propto (p_2 - p_1)$, implying that the asymmetric capillary force increases with increasing the pitch difference. When the designed asymmetric capillary force f_j is large enough to overcome all other random effects, the collapse is directed.

This concept can be extended to a two-dimensional array of pillars. We designed a periodic two-dimensional 4-pillar-unitcell array of nanopillars, as shown in Fig. 1d(III). We fixed the intracell pitch p_1 and varied the intercell spacing p_2. When p_2 was greater than p_1, the asymmetric capillary force of each pillar pointed to the center of its cell. We patterned an array of nanopillars in PMMA using a negative-tone electron-beam lithography (EBL) process. After development in developer and rinsing in IPA, the negative PMMA nanopillars were spin-dried. The intracell pitch p_1 was 50 nm, the pillars were ~80 nm tall, and the diameter was ~ 20 nm. The intercell spacing p_2 varied from 50 nm to 90 nm.

In the case of $p_2 = p_1$ shown in Fig. 1e, the pillars collapsed randomly and formed different assemblies consisting of between 2 and 9 elements. As p_2 increased, the yield of the intended intracell 4-pillar collapse increased correspondingly (Figs. 1f-1g), indicating that the collapse of the pillars were more directed and controllable. Once p_2 was large enough, the yield reached 100%, as shown in Fig. 1h, where $(p_2 - p_1)$ was 8 nm, i.e. a 16% increase relative to the intracell pitch p_1. The yield as a function of (p_2-p_1) is shown in Fig. 1i, from which we can see a clear systematic trend.

To further demonstrate the reliability of this strategy, we designed a series of multi-element cells with different cell geometries. Figs. 2a-2f show that assemblies with 2, 3, 4, 6, 7, and 9 elements in each cell nanocohered as designed, where the intercell spacing p_2 was ~ 2 times that of the intracell pitch p_1, and all other parameters were the same as those in Figs.1e-h. In these assemblies, we can see that all boundary pillars in any single cell cohered to the center of the cell rigidly, while the middle pillars (in 7- and 9-element cell, shown in Figs. 2e and 2f, respectively) remained vertical because of symmetry within the cell. No imperfections were found across ~ 16 μm^2 patterns (400 cells, our largest test area for this sample).

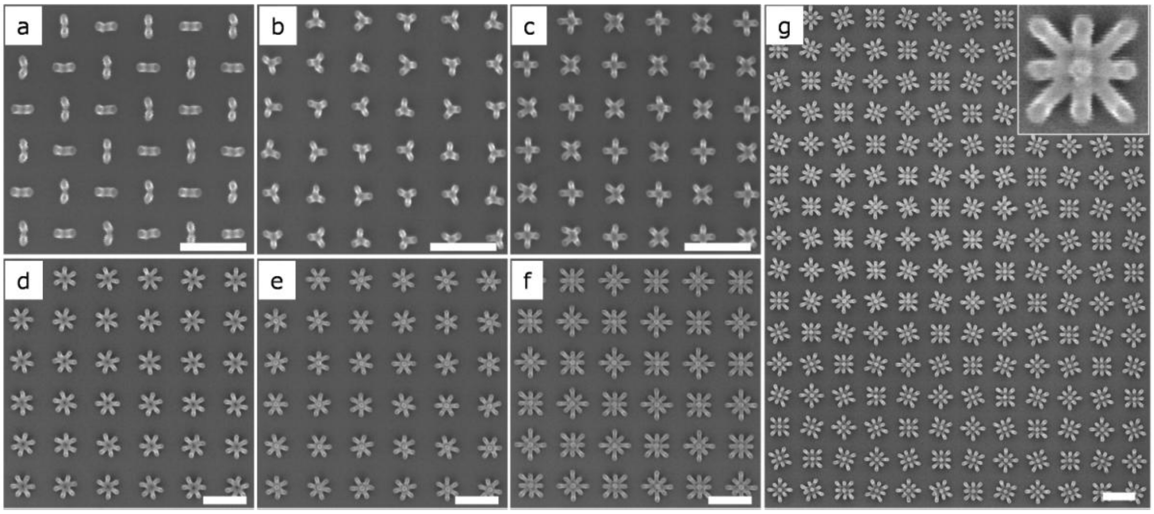

Figure 2. SEM images of ordered multi-element assemblies fabricated by capillary-force-induced nanocohesion. (**a**) 2-element-cell with two different rotations; (**b**) 3-element-cell with three different rotations; (**c**) 4-element-cell with two different rotations; (**d**) 6-element-cell with three different rotations; (**e**) 7-element-cell with three different rotations; (**f**) 9-element-cell with two different rotations; and (**g**) large area 9-element-cell with four different rotations. The diameter of nanopillars was ~ 20 nm, the pitch of pillars in the cell was 50 nm, and the intercell spacing between adjacent cells was ~ 100 nm. The thickness of PMMA was ~ 90 nm and the resultant negative PMMA nanopillars were ~ 80 nm tall. All scale bars are 200 nm.

Fig. 2g shows a new type of example in which 9-pillar-cell arrays with 4 different rotations were self-assembled, from which we can see robustly ordered assemblies were achieved by capillary-force-induced nanocohesion. This nanocohesion-based self-assembly could also be achieved across a range of length scales with different materials and geometries (Fig. S1-S3).

Though we could get robust ordered assemblies for small-element-number cells because the asymmetric capillary force was large enough to direct cohesion for all pillars, the assembly of larger-element-number (>25) uniform cells was more difficult (Fig. 1c and Fig. S4) because the lower asymmetric capillary force for inner pillars permitted random collapse. For this case, we describe here that directed self-assembly could still be realized by controlling the critical minimum cohesion force $f_{\min}$ through varying the dot exposure dose during the lithography process (and thus varying the pillar diameter and perhaps also slightly varying its intrinsic strength).

For a given pitch, the critical minimum cohesion force[33] is given by

$$f_{\min} \sim Ed^4/h^3 = Ed/A^3 = Eh/A^4 \qquad (5)$$

where E is Young's modulus, d is the diameter of the pillar, h is the height of the pillar, and A is the aspect ratio of the pillar defined by $A = h/d$. This formula implies that to decrease $f_{\min}$, we can increase the elasticity (i.e., decrease E), decrease the diameter d, or increase the height h. When elasticity variation is negligible, increasing aspect ratio A is the most effective way to decrease $f_{\min}$.

To engineer $f_{\min}$, we fabricated a uniform 171-element array of hexagonal high-aspect-ratio negative PMMA nanopillars. The height of the pillars h was ~ 550 nm, and the pitch p was 200 nm. The diameter d of pillars was controlled by changing the exposure dose of each pillar, which allowed us to achieve varying aspect ratios. Figs. 3a-3d shows the evolution of nanocohesion of this 171-element nanopillar array as the aspect ratio was increased by decreasing lithographic electron exposure. From these figures, we can see that with decreasing pillar diameter, pillars tended to cohere towards the pattern center.

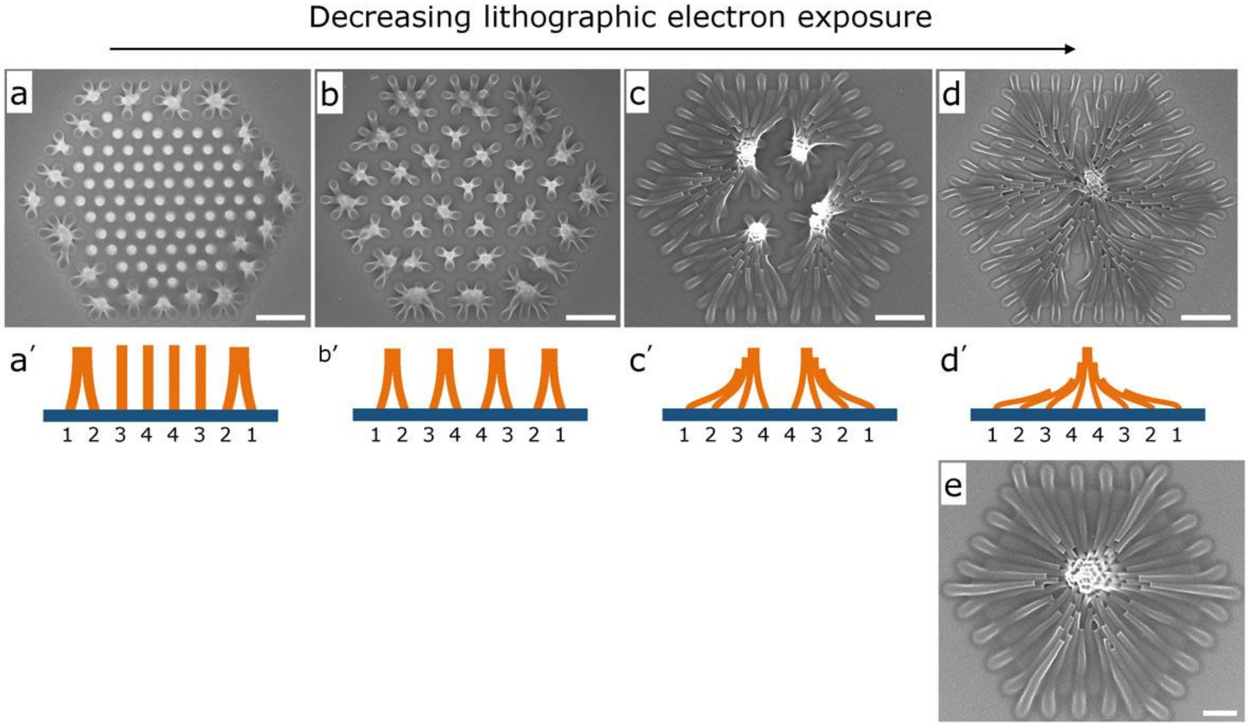

Figure 3. SEM images of large-element-number assemblies fabricated by capillary-force-induced nanocohesion. (**a-d**) SEM images of the evolution of a 171-pillar array with increasing the aspect ratio by decreasing lithographic electron exposure dose: (**a**) 5.7 pC/pillar, (**b**) 4.0 pC/pillar, (**c**) 2.8 pC/pillar, and (**d**) 2.0 pC/pillar, showing how asymmetric capillary force determined nanocohesion of a large array with different aspect ratios. The pitch of the pillars was 200 nm. The scale bars are 500 nm. (**a'-d'**) Cross-sectional schematic diagrams of different scenarios for (a-d). (**e**) SEM image of a symmetric nanohill collapsed from a 91-pillar array (smaller than in cases a-d) with a pitch of 160 nm by nanocohesion. Scale bar is 200 nm. The PMMA thickness was ~ 600 nm and resultant height of nanopillars was ~ 550 nm.

We can use the theoretical picture described above to give a qualitative explanation of the dynamic process of each scenario. To illustrate the process, we consider a uniformly spaced one-dimensional 8-nanopillar array, shown schematically in Figs. 3a'-3d', in which the initial asymmetric capillary forces for each nanopillar are f_1, f_2, f_3, and f_4, and $f_1 > f_2 > f_3 > f_4$ according to our model. Suppose the critical minimum lateral cohesion forces for each of the pillars in Figs. 3a-3d were f_a to f_d. With decreasing the diameter, from formula (5), we know $f_a > f_b > f_c > f_d$. In the first case (Fig. 3a), we believe the initial condition was $f_1 > f_a > f_2 > f_3 > f_4$, so pillar 1 collapsed first. During the collapse of pillar 1, the distance between pillar 1 and pillar 2 decreased and the capillary force between them increased dramatically ($f \sim 1/p_{12}$), which made f_2 reverse in directions and increase in magnitude so that it induced pillar 2 to collapse towards pillar 1 (we describe this dynamic interaction as a "domino effect"); after pillar 2 collapsed, the asymmetric capillary forces for pillar 3 and pillar 4 increased but were still smaller than the critical force f_a required to induce the collapse (Fig. 3a'). In the second case (Fig. 3b), the initial condition was also $f_1 > f_b > f_2 > f_3 > f_4$, so that pillar 1 collapsed and induced pillar 2 collapse towards pillar 1 as in the first case. However, in contrast to the first case, during the collapse process of pillar 2, the asymmetric capillary force for pillar 3 was now sufficient to collapse pillar 3 towards pillar 4, and another domino effect took place for the remaining pillars (Fig. 3b'). In the third case (Fig. 3c), we understand $f_1 > f_2 > f_3 > f_c > f_4$, so pillar 1, 2, and 3 initially collapsed to the center and induced pillar 4 to collapse to pillar 3 (Fig. 3c'). In the last case (Fig. 3d), the initial asymmetric capillary force of all pillars was such that $f_1 > f_2 > f_3 > f_4 > f_d$, so that all of them collapsed to the center (Fig. 3d'). The above-mentioned dynamic processes were also found in non-uniform pillar arrays, shown in Fig. S5.

More symmetric assemblies could be obtained from smaller arrays, as shown in Fig. 3e and Fig. S6, where hexagonal nanopillar arrarys were assembled into symmetric nanohills. This symmetry was possible because the asymmetric capillary force for the pillar nearest to the middle should be $f_N \sim 1/Np$ according to equation (3), so for fewer-element pillar arrays, pillars closer to the middle should be more easily directed compared to larger arrays. We also noticed that although increasing the aspect ratio could increase the fidelity of self-assembly, the collapse of nanopillars would be partly determined by random effects when the aspect ratio was too high, resulting in random collapse of some pillars (see Fig. S7). In this case, we believe that the critical lateral collapse force $f_{\min}$ was so small that it was comparable with random forces induced by imperfections and self-weight of pillars, so random forces partly affected the collapse.

As described above, the action of nanocohesion was determined by the relationship of designed asymmetric capillary force and the critical collapse force $f_{\min}$ of nanopillars. By deliberately setting this relationship for all the nanopillars in a pattern, we also showed that complex hierarchical nanostructures could be fabricated by nanocohesion as is evident in Fig.4.

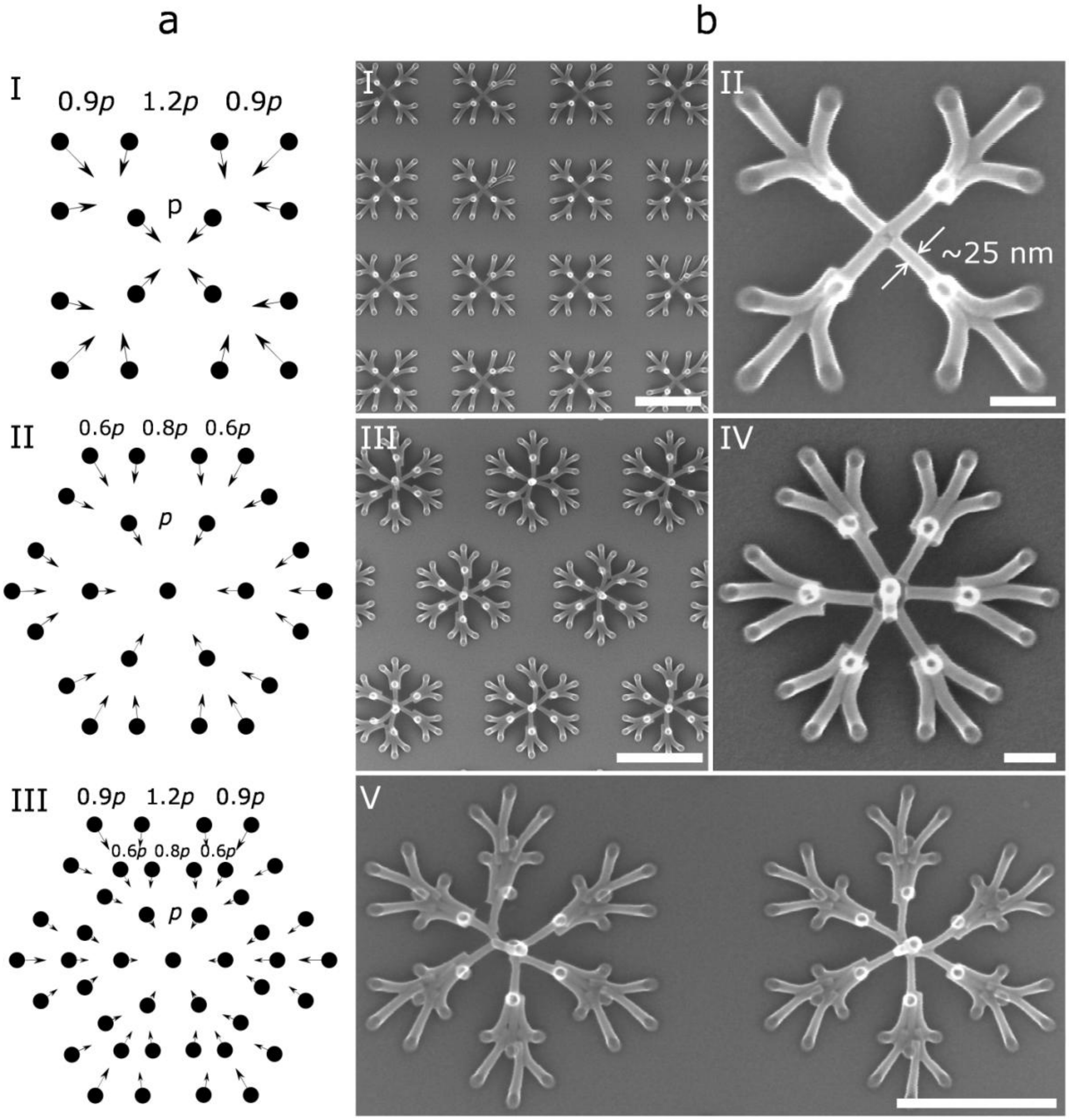

Figure 4. SEM images of hierarchical assemblies fabricated by capillary-force-induced nanocohesion. (**a**) Schematics of simple hierarchical designs using 16 (I), 25 (II), and 43 (III) pillars. (**b**) SEM images of symmetric hierarchical networks collapsed from the designs in (a), with *p* value of 150 nm. The scale bars for b(I, III, V) are 500 nm, for b(II and IV) are 100 nm. The diameter of PMMA nanopillars was ~25 nm. The thickness of PMMA here was ~ 250 nm and the resultant height of nanopillars was ~ 220 nm.

Fig. 4a shows some hierarchical designs where the basic concept was to deliberately vary the local position (by ~10%, relative to a uniform distribution) of some pillars in a larger cell to create controlled sub-structures. Thus, while boundary pillars in the cell had the largest capillary force, the pillars in the designed sub-structures also had sufficient capillary forces to induce directed collapse, as shown schematically by the arrows in Fig. 4a. Fig. 4b shows complex hierarchical networks fabricated on the basis of the designs in Fig. 4a, from which we can see that the pillars collapsed and self-assembled in the expected directions to form the desired patterns. Though the yield decreased when increasing the total element-number in these tests, we believe this technique could be further improved by optimizing the pillar placement and geometry.

The central result of this report is the demonstration of a new nanoassembly strategy based on capillary-force-induced cohesion of high-aspect-ratio nanostructures during the post-development drying process. By using this strategy, robust ordered complex networks of nanostructures were fabricated. Though we focused here on patterning with electron-beam-lithography, we believe that this technique can be also applied to other high-aspect-ratio nanostructures, including functional vertically-aligned semiconductor nanowires or nanorods, carbon nanotubes, or metal nanopillars to perhaps permit functional self-assembled structures. On the other hand, from a lithographier's point of view, this self-assembly technique suggests a number of potential applications in electron-beam lithography, including: (1) increasing the throughput by patterning only a portion of the final structures, then increasing the pattern area by inducing controlled collapse; (2) reducing proximity effect[34] by reducing the total dose needed to make patterns in a given area (again by patterning only pillars, then inducing collapse to make linear structures); and (3) reducing electron exposure in radiation-sensitive devices by using induced collapse across sensitive device material to define a device feature. Additionally, because the process can take place at sub-20-nm scale, this technique could also serve as a platform for scientific investigation of fluid flow near the molecular scale to study the mechanism of evaporation, dewetting phenomena, and the mechanical behaviors of structures on the 10-nm length scale.

Acknowledgement

This work was supported by Office of Naval Research and Nanoelectronics Research Initiative. Patterning was done at MIT's shared scanning-electron-beam-lithography facility in the Research Laboratory of Electronics. We thank M. Mondol and J. Daley for technical assistance. H. G. Duan was supported by a fellowship from the China Scholarship Council.

References

1. de Gennes, P.G.; Brochard-Wyard, F.; Quere, D. *Capillarity and Wetting Phenomena: Drops, Bubbles, Pearls, Waves* (Springer, New York, 2003).
2. Bico, J.; Roman, B.; Moulin, L.; Boudaoud, A. *Nature* **2004**, 432**,** 690.
3. Kim, H. Y.; Mahadevan, L. *J. Fluid Mech.* **2006**, 548, 141-150.
4. Gao, X. F.; Jiang, L. *Nature* **2004**, 432**,** 36.
5. Geim, A. K.; Dubonos,S. V.; Grigorieva, I. V.; Nonoselov, K. S.; Zhukov, A. A.; Shapoval, S. Yu. *Nature Mater.* **2003**, 2, 461-463.
6. Blossey, R. *Nature Mater.* **2003**, 2, 301-306.
7. Guo, J. G.; Zhou, L. J.; Zhao, Y. P. *J. Colloid Interface Sci.* **2009**, 331, 458-462.
8. Ahn, M.; Heilmann, R. K.; Schattenburg, M. L. *J. Vac. Sci. Technol. B* **2007**, 25, 2593-2597.
9. Yin, Y. D.; Lu, Y., Gates, B.; Xia, Y. N. *J. Am. Chem. Soc.* **2001**, 123, 8718-8729.
10. Kraus, T.; Malaquin, L.; Schmid, H.; Riess, W.; Spencer, N. D.; Wolf, H. *Nature Nanotech.* **2007**, 2, 570-576.

11. Peyrade, D.; Gordon, M.; Hyvert, G.; Berton, K.; Tallal, J. *Microelectron. Eng.* **2006**, 83, 1521–1525.
12. Cui, Y.; Björk, M. T.; Liddle, J. A.; Sönnichsen, C.; Boussert, B.; Alivisatos, A. P. *Nano Lett.* **2004**, 4, 1093-1098.
13. Rothemund, P. W. *Proc. Natl. Acad. Sci.* **2000**, 97, 984-989.
14. Bowden, N.; Terfort, A.; Carbeck, J.; Whitesides, G. M. *Science* **1997**, 276, 233-235.
15. Py, C.; Reverdy, P.; Doppler, L.; Bico, J.; Roman, B.; Baroud, C. N. *Phys. Rev. Lett.* **2007**, 98, 156103.
16. Guo, X. Y.; Li, H.; Ahn, B. Y.; Duoss, E. B.; Hsia, K. J.; Lewis, J. A. *Proc. Natl. Acad. Sci.* **2009**, 106, 20149-20154.
17. Jacobs, H. O.; Tao, A. R.; Schwartz, A.; Gracias, D. H.; Whitesides G. M. *Science* **2002**, 296**,** 323-325.
18. Pokroy, B.; Kang, S. H.; Mahadevan, L.; Aizenberg, J. *Science* **2009**, 323, 237-240.
19. Cohen, A. E.; Mahadevan, L. *Proc. Natl. Acad. Sci.* **2003**, 100, 12141-12146.
20. Neukirch, S.; Roman, B.; de Gaudemaris, B.; Bico, J. *J. Mech. Phys. Solids* **2007**, 55, 1212-1235.
21. Duan, H. G.; Zhao, J. G.; Zhang, Y. Z.; Xie, E. Q.; Han, L. *Nanotechnology* **2009**, 20**,** 135306.
22. Lau, K. K. S. *et al. Nano Lett.* **2003**, 3, 1701-1705.
23. Dev, A.; Chaudhuri, S. *Nanotechnology* **2007**, 18**,** 175607.
24. Zhao, Y. P.; Fan, J. G. *Appl. Phys. Lett.* **2006**, 88, 103123.
25. Chandra, D.; Yang, S.; Soshinsky, A. A.; Gambogi, R. J. *Appl. Mater. Interfaces* **2009**, 1, 1698-1704.
26. Tanaka, T.; Morigami, M.; Atoda, N. *Jpn. J. Appl. Phys.* **1993**, 32, 6059-6064.
27. Zhang, Y.; Lo, C. W.; Taylor, J. A.; Yang, S. *Langmuir* **2006**, 22*,* 8595-8601.
28. Hui, C. Y.; Jagota, A.; Lin, Y. Y.; Karmer, E. J. *Langmuir* **2002**, 18, 1394-1407.
29. Pokroy, B.; Epstein, A. K.; Persson-Gulda, M. C. M.; Aizenberg, J. *Adv. Mater.* **2009**, 21, 463-469.
30. Wu, D.; *Chen, Q. D.; Xu, B. B.; Jiao, J.; Xu, Y.; Xia, H.; Sun, H. B. Appl. Phys. Lett.* **2009**, 95, 091902.
31. Sidorenko, A.; Krupenkin, T.; Taylor, A.; Fratzl, P.; Aizenberg, J. *Science* **2007**, 315, 487-490.
32. Israelachvili, J. N. *Intermolecular and Surface Forces* (Academic Press Ltd., London, 2nd ed., 1992).
33. Beer, F. B.; Johnston, E. R. *Mechanics of Materials* (2nd ed. McGraw-Hill, New York, 1992).
34. Chang, T. H. P. *J. Vac. Sci. Technol.* **1975**, 12, 1271-1275.

Supplemental Information

Directed Self-assembly by Using Capillary-Force-Induced Nanocohesion

Huigao Duan[1, 2], Karl K. Berggren[1, *]

[1] Department of Electrical Engineering and Computer Science, Massachusetts Institute of Technology, Cambridge, MA 02139, USA

[2] School of Physical Science and Technology, Lanzhou University, Lanzhou, Gansu 730000, P. R. China

[*] To whom correspondence should be addressed, E-mail: berggren@mit.edu

Section S1. Methods

Poly (methyl methacrylate) (PMMA) resist (950K, in anisole) from MicroChem Corp. was used in experiments. PMMA was spin-coated on silicon substrates for exposure. Different-thickness PMMA (including 93 nm, 250 nm, and 600 nm for different experiments) was achieved by controlling the concentration of PMMA resist in anisole and changing the spinning speed. After spin-coating, PMMA was baked on a hot plate at 170°C for 90 seconds to flatten the film, get rid of residual solvent, and enhance the adhesion between PMMA and the substrate. The thickness of PMMA was measured by an ellipsometer.

Electron-beam lithography (EBL) was done on a Raith 150 tool at 30 kV acceleration voltage, ~6 mm working distance, and ~400 pA beam current. To obtain negative PMMA pillars (*S1*), a dose range from 0.2 pC to 6 pC was used for each designed single-pixel dot. The diameter of negative PMMA pillars was controlled by electron dose for each dot. After exposure, the samples were developed in 1:2 Methyl isobutyl ketone (MIBK): isopropyl alcohol (IPA) for 1 min at 20°C and subsequently rinsed by pure IPA. After rinsing, a sample was critical-point dried in pure ethanol by a critical point dryer (Tousimis Autosamdri-815B) to study how capillary force affected the collapse of high-aspect-ratio nanopillars. Other samples for self-assembly were dried by a spinner at 1800 rpm in air at room temperature (~ 20°C).

The morphology of all samples was observed using a Raith 150 SEM operated with an acceleration voltage of 10 kV and working distance of ~ 6 mm. No metal layer was sputter-coated on samples before imaging.

Section S2. Supporting Figures

Fig. S1: Self-assembly of 10-nm-scale hydrogen silsesquioxane (HSQ) dots by capillary-force-induced nanocohesion

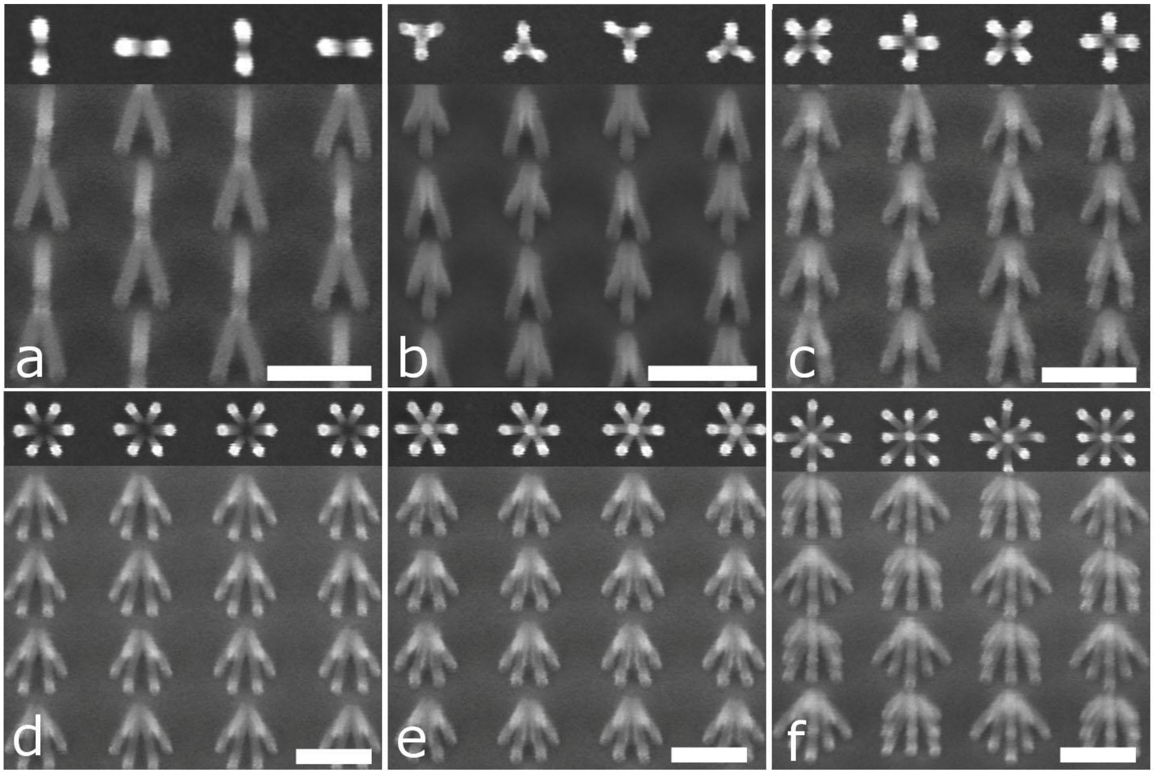

Fig. S1. Side view scanning electron microscopy (SEM) images of self-assembled hydrogen silsesquioxane (HSQ) nanopillars. The sample was tilted 45° during imaging to observe three-dimensional morphologies, and the insets in (a-f) are their corresponding top view images. The diameter of HSQ pillars was ~15 nm, the thickness of HSQ was ~ 100 nm, the intracell pitch of pillars prior to cohesion in a cell was 40 nm, and the spacing between two adjacent cells was ~80 nm. The exposure was done by a Raith 150 scanning electron-beam lithography tool with an accelerating voltage of 30 kV. The sample was developed by a salty developer (*S2*) for 4 min at 24°C, rinsed in deionized water for 2 minutes, and subsequently rinsed by isopropyl alcohol (IPA). The sample was spin-dried at 1800 rpm in air at room temperature. Scale bars, 100 nm.

Fig. S2: Large area nanocohesion of 220-nm-height negative PMMA nanopillars

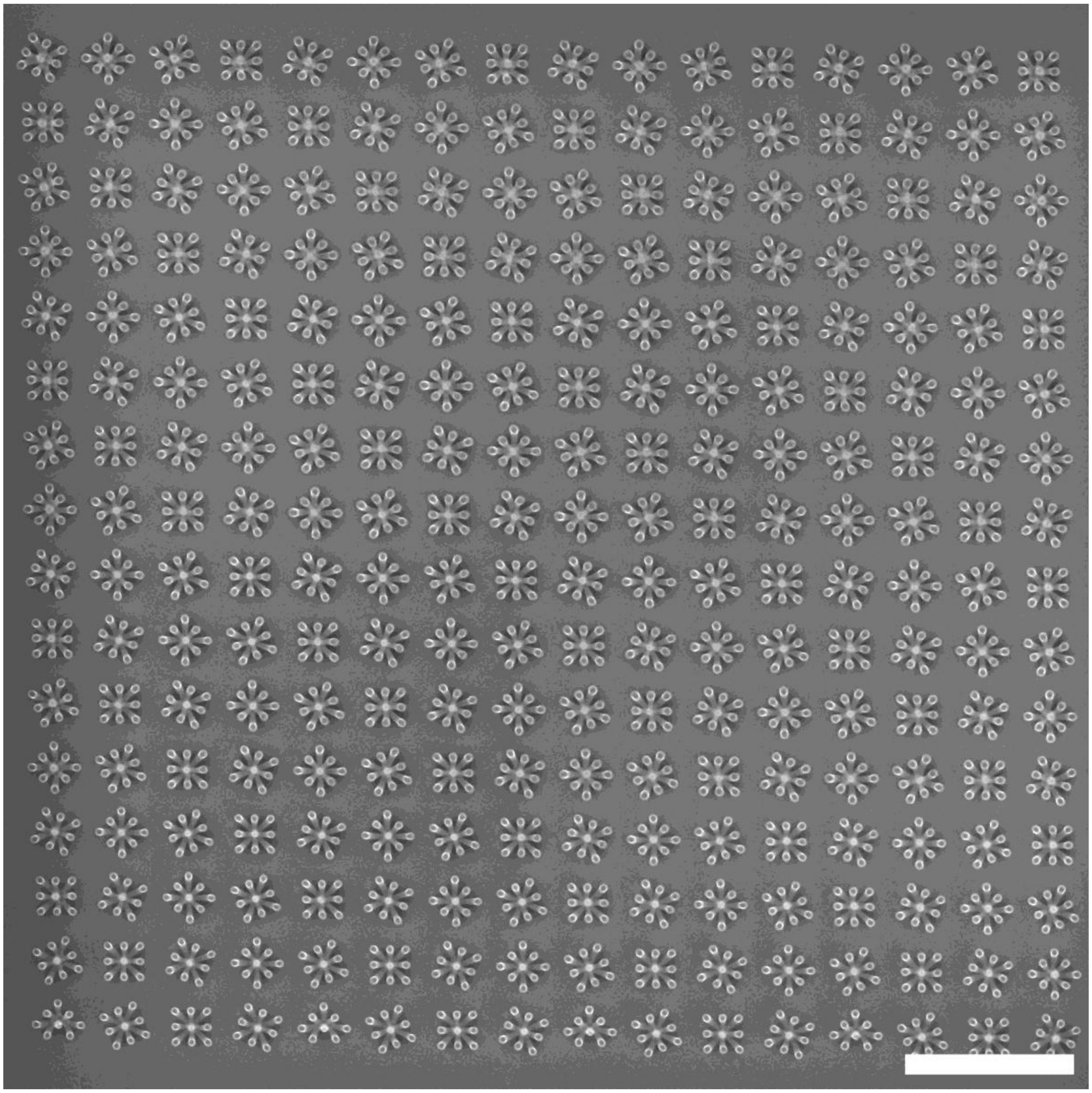

Fig. S2. SEM image of a highly-ordered large-area (~36 μm^2) self-assembled 220-nm-height negative PMMA nanopillars fabricated by capillary-force-induced nanocohesion. The diameter of nanopillars was ~30 nm, the electron dose of each pillar was ~1.5 pC. The intracell pitch was 100 nm, and the spacing of two adjacent cells was 200 nm. Scale bar, 1 μm. Note that there were several pillars missing at the bottom of the pillar array because these pillars were on the boundary of a write field in the exposure process where errors occur when the beam deflection is too fast.

Fig.S3. Capillary-force-induced nanocohesion of 220-nm-tall PMMA nanopillars and their cross-sectional images.

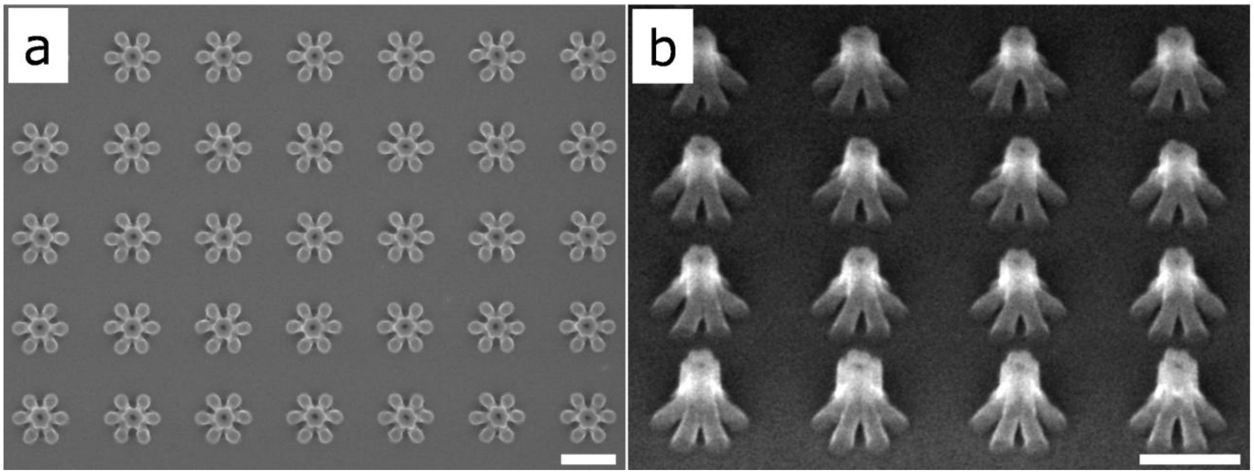

Fig. S3. SEM image of an array of cohered 220-nm-tall PMMA nanopillars: (a) top view, (b) tilted view. The intracell pitch was 80 nm. Scale bar, 200 nm.

Fig. S4: Increasing the pillar number in a single cell resulted in the failure of nanocohesion

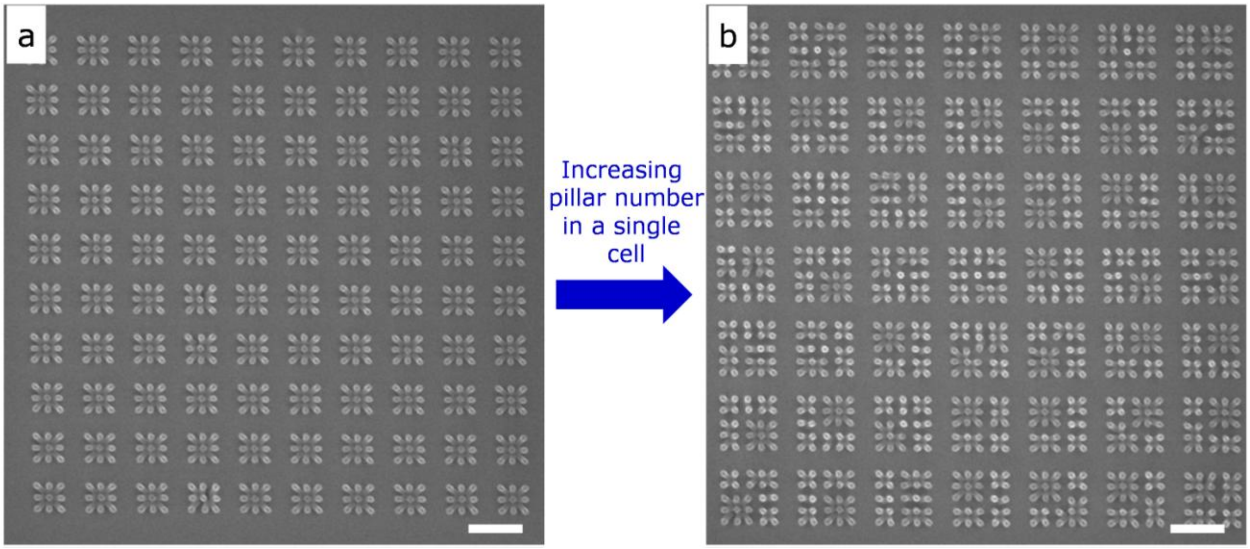

Fig. S4. SEM images of self-assembly of negative PMMA nanopillars by capillary-force-induced nanocohesion: (**a**) 9 pillars per cell, (**b**) 25 pillars per cell. With the same aspect ratio, increasing pillar number in a single cell resulted in the failure of nanocohesion. The height of PMMA was ~80 nm, intracell pitch was 50 nm, intercell spacing was 100 nm.

Fig. S5. Dynamic process of nanocohesion from non-uniform pillar arrays

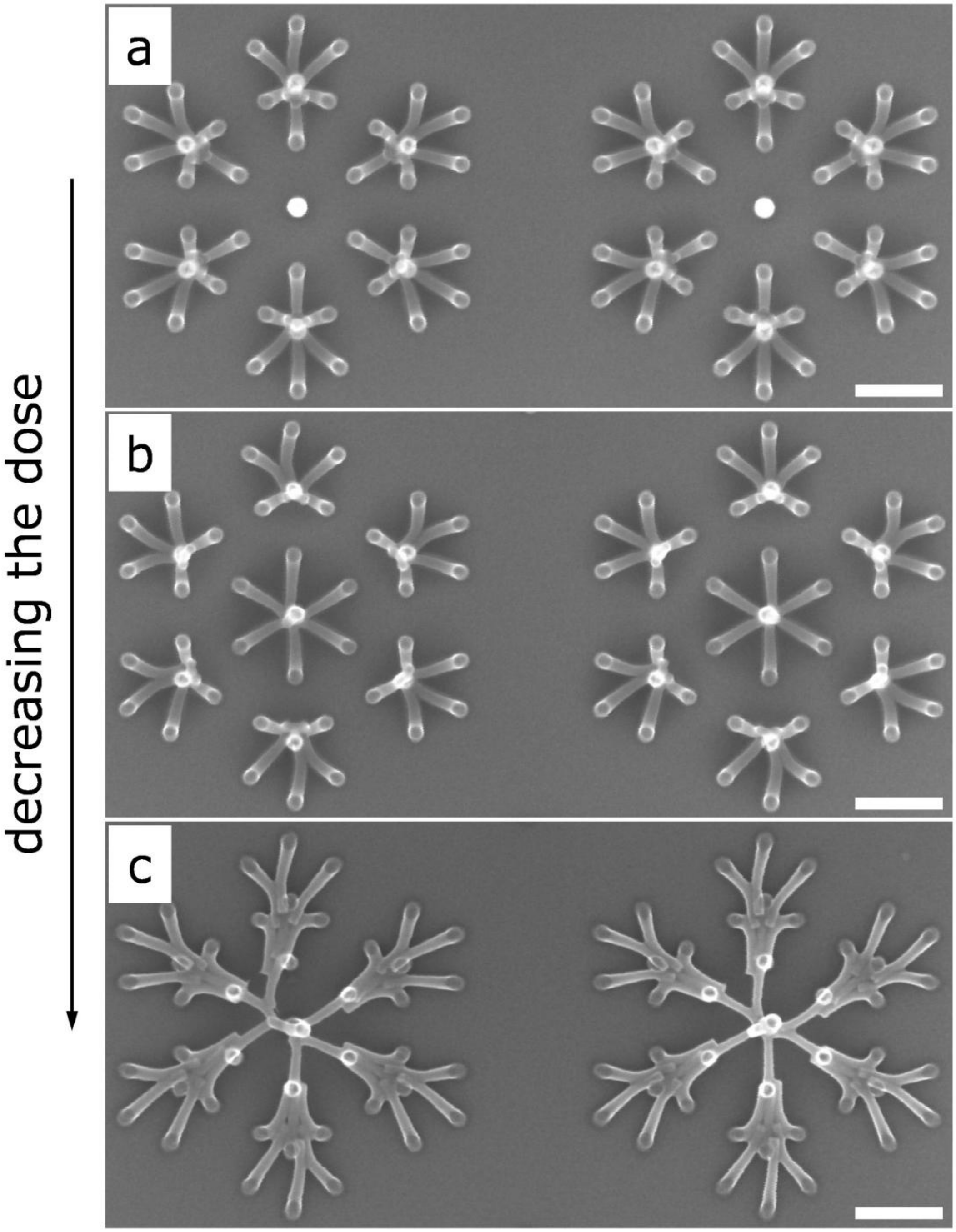

Fig. S5. SEM images of the evolution of a 43-pillar array with increasing the aspect ratios by decreasing the dose: (**a**) 1.5 pC/pillar, (**b**) 1.3 pC/pillar, and (**c**) 1.1 pC/pillar, showing the dynamic processes of nanocohesion of a large array with different aspect ratios. The height of pillars was ~220 nm. Scale bars, 200 nm.

Fig. S6: Large area nanohills cohered from 61-element negative PMMA nanopillar arrays by capillary forces.

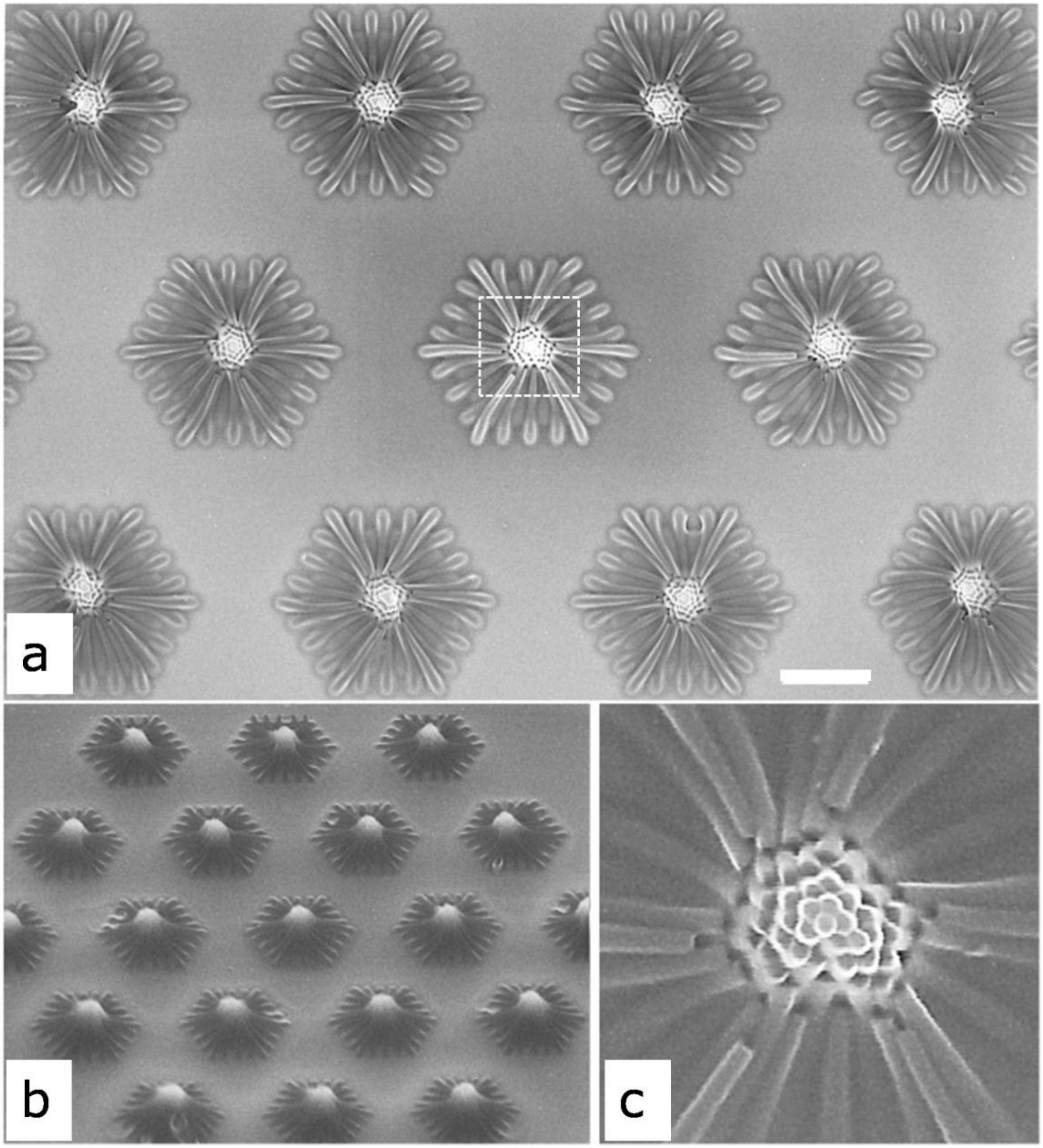

Fig. S6. SEM images of an array of nanohills cohered from 61-element negative PMMA nnaopillar arrays, (**a**) top view, (**b**) 45° tilted view, and (**c**) enlarged image of the top part of a nanohill. The height of the negative PMMA pillars was ~550 nm, with diameter of ~50 nm. The intracell pitch of pillars was 160 nm. Scale bar in (a), 500 nm.

Fig. S7: For very large aspect ratio, some random collapse of nanopillars occurred.

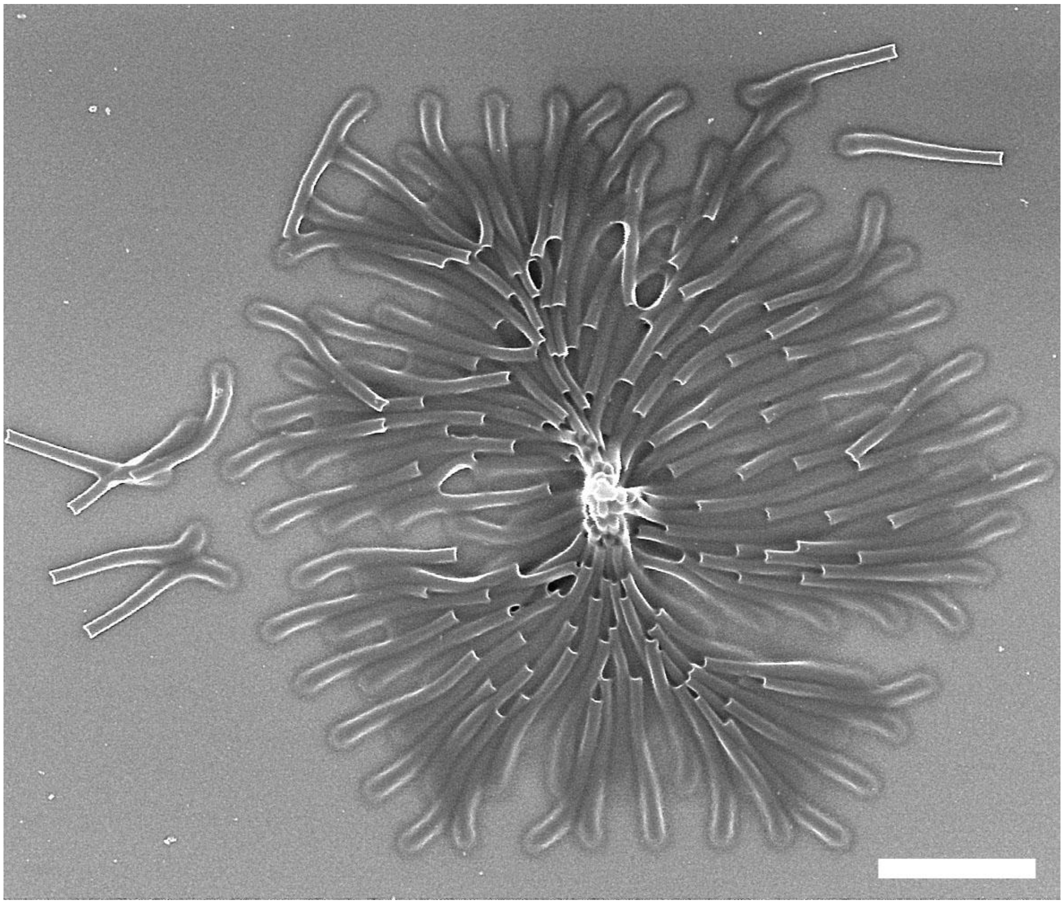

Fig. S7. SEM image of nanocohesion from a 171-element ultra-high-aspect-ratio negative PMMA nanopillar array. The height of PMMA nanopillars was ~550 nm, the electron-dose for each pillar was ~1.5 pC. The pitch of nanopillars was 200 nm. Scale bar, 500 nm. Very large aspect ratio resulted in some random collapse of nanopillars because the critical collapse force of nanopillars was too small. When the critical collapse force was too small, some random forces from self-weight and imperfections of nanopillars could be comparable as the critical collapse force, resulting in random collapse.

References:

S1. H. G. Duan, J. G. Zhao, Y. Z. Zhang, E.Q. Xie, L. Han, *Nanotechnology* **20,** 135306 (2009).

S2. Joel K. W. Yang, Karl K. Berggren, *J. Vac. Sci. Technol. B* **25**, 2025 (2007).